

Experimentally-Derived Bidirectional Reflectance Distribution Function Data in Support of the Orbital Debris Program Office

J. Hostetler

Jacobs, NASA Johnson Space Center, MC XI5, 2101 NASA Pkwy, Houston, TX 77058, USA

H. Cowardin

Jacobs, NASA Johnson Space Center, MC XI5, 2101 NASA Pkwy, Houston, TX 77058, USA

ABSTRACT

The NASA Orbital Debris Program Office (ODPO) has used various optical assets to acquire photometric data of Earth-orbiting objects to define the orbital debris environment. To better characterize and model optical data acquired from ground-based telescopes, the Optical Measurements Center (OMC) at NASA Johnson Space Center emulates illumination conditions seen in space by using equipment and techniques that parallel telescopic observations and source-target-sensor orientations.

One of the OMC goals is to improve the size calculation used for optical data by developing an optical-based Size Estimation Model. The current size estimation requires applying a Lambertian phase function, a set albedo value, and range to the observed magnitude. The first step to improving the sampled brightness of laboratory targets is to remove aspect-angle dependencies. Then, the volume of possible object viewing angles is sampled at 21 combinations of azimuth and zenith angles for each solar phase angle. Finally, the acquired images are input into an image processing program that generates approximations for the object's Bidirectional Reflectance Distribution Function (BRDF) and phase function. The BRDF is a radiometric concept that identifies an object's material composition by matching a BRDF approximated with photometric data collected by ground-based telescopes with a BRDF generated experimentally from a known object in the laboratory.

This paper discusses the validation of experimental BRDF and phase function approximations produced in the OMC and how the findings will be incorporated into ODPO models. A Lambertian sphere is imaged and the subsequent experimental functions are scrutinized to confirm that they correspond to an object that has an isotropic luminance. With the image processing algorithm validated, test objects with varying optical properties are then imaged to confirm that the produced photometric functions are both unique and repeatable. Once the validation is complete, the OMC will be used to evaluate a subset of fragments from a hypervelocity impact test of a mock-up satellite and assess the appropriate phase function and size estimates using BRDF measurements for a large volume of targets composed of various shapes, sizes, and materials.

1. INTRODUCTION

The NASA Orbital Debris Program Office (ODPO) has utilized optical observations of Earth-orbiting objects to better characterize the orbital debris environment. Ground-based measurements provide time-dependent orbital parameters and brightness (i.e., magnitudes). The magnitude data is converted into size assuming a range, phase function, and albedo. Capitalizing on optical data products, using laboratory measurements acquired in the Optical Measurements Center (OMC), and applying them to generate a more complete understanding of orbital space objects is a key objective of NASA's Optical Measurements Program. The OMC is used to emulate space-based illumination conditions using equipment and techniques that parallel telescopic observations and source-target-sensor orientations.

To minimize the uncertainties in the size estimation, laboratory data is critical to better characterize ground-based measurements. Laboratory data provides a target's known shape, size, and material that can be used to investigate phase functions and albedo to improve the current size estimation using optical measurements.

The following presents the latest capabilities using Bidirectional Reflectance Distribution Function (BRDF) measurements, which remove any aspect angle dependence and provide preliminary phase function measurements from a simple sphere shape of different materials. The paper reviews the validation of the experimental BRDF data

and provides a path forward for assessing phase function distributions and improving the size estimation model (SEM) currently used for telescopic observations.

2. DATA ACQUISITION / INSTRUMENTATION

The OMC's design is analogous to a telescope set-up with a light source, target, and observer. A 75W, Xenon arc lamp simulates solar illumination from 200 nm to 2500 nm. The data are acquired through a Santa Barbara Instrument Group charge-coupled device (CCD) camera (1024 x 1536 pixels) with an attached filter wheel that uses the standard astronomical suite of Johnson/Bessel filters: Blue (B), Visible (V), Red (R), Clear (C) and Infrared (I). The laboratory equipment is capable of obtaining data for a full 360° range in phase angle (the vertex angle between light source, object, and detector) with an accuracy of 1° using a custom-built rotary arm with attached, commercial off-the-shelf potentiometer. To prevent scattered light from biasing the observations, a light trap (not shown) is placed directly across from the light source on the other end of the rotary arm; therefore, the data is limited to phase angles between ±(3°- 160°). The layout is shown in Fig.1 with small digital images of the equipment. The target is oriented at the end of a robotic arm, recently improved with the addition of a sixth degree of freedom that enables the target to be viewed at any desired orientation. A 3D-printed polylactic acid end effector was also designed and implemented to eliminate as much interference as possible from light scattering off of the robotic arm.

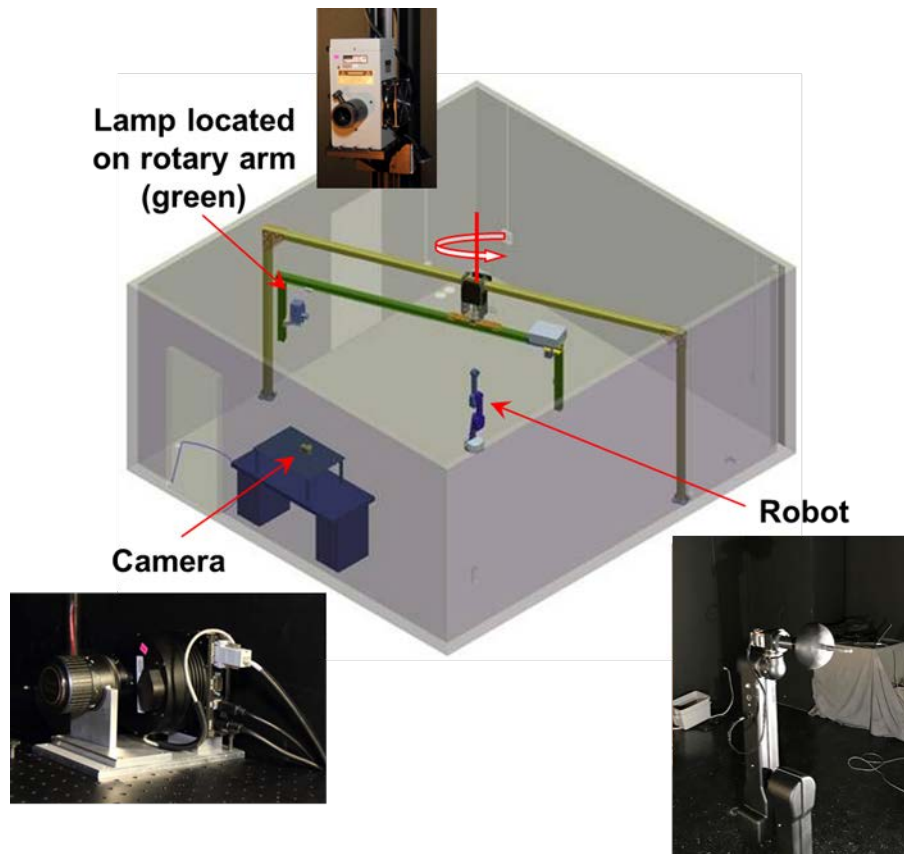


Fig. 1. OMC Experimental Setup [1]

The principal objective of this work is to improve the accuracy of size calculations used for optical data by developing an optical-based SEM. The accepted method for determining the size of orbital debris from optical measurements, as proposed by Barker et al.[2], is formulated as follows:

$$d = \frac{2R}{[\pi\alpha_g f(\phi)]^{1/2}} \times 10^{\left[\frac{M_{abs}(\gamma) + M_{sun}(\gamma)}{-5} \right]}$$

(1)

where d is the diameter of the object; R is the distance from the observer to the object; α_g is the object's geometric albedo; M_{abs} is the apparent brightness of the object normalized to a standard distance, R_o ; M_{sun} is the Sun's apparent brightness normalized to R_o ; f is an attenuation function dependent on the solar phase angle, ϕ , and is specific to the particular shape of the object; and γ is the bandpass. While many of the quantities used in Eq. 1 are readily accessible via photometric analysis, the quantities α_g and $f(\phi)$ are un-discernable and/or un-knowable when tracking an object with a telescope. This necessitates assumptions be made to approximate a solution; mainly that the phase function, $f(\phi)$, be Lambertian and the albedo have a set value. Therefore, to improve the size estimations produced by Eq. 2, the OMC intends to supplement approximations for α_g and $f(\phi)$, which are generated in lab from representative samples of orbital debris imaged at a fixed distance.

To improve the sampled brightness of laboratory targets, the aspect-angle dependencies in these measurements is removed by fixing the object to the end effector of a six degree-of-freedom robotic arm and sampling a hemisphere of object view orientations. The totality of this sampled hemisphere is analogous to the BRDF, defined by Nicodemus et al.[3], as a radiometric concept that identifies the reflective characteristics of a surface by the ratio of reflected radiance in the direction (Θ_r, Ψ_r) to the radiation flux incident on a surface from direction (Θ_i, Ψ_i) within the solid angle element $d\omega_i$ (Fig. 2).

$$f_r(\theta_i, \phi_i; \theta_r, \phi_r; E_i) = \frac{dL_r(\theta_r, \phi_r; \theta_i, \phi_i; E_i)}{L_i(\theta_i, \phi_i) \cos \theta_i d\omega_i} \quad (2)$$

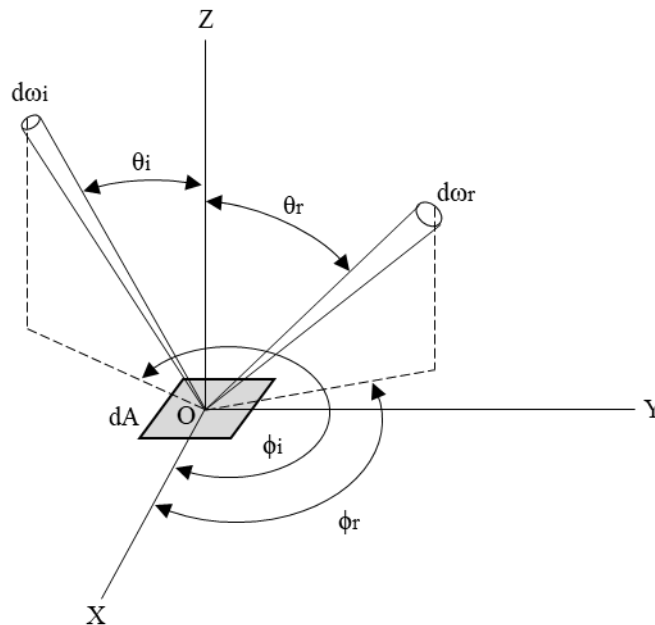


Fig. 2. Ray geometry for the BRDF of a differential element

To adapt this concept to astronomic photometry, the BRDF approximations generated in the OMC replace radiance with the illuminance ratio for a space object, described generally as:

$$\frac{E_r}{E} = \frac{k\alpha A}{R^2} f(\phi) \quad (3)$$

where E is the radiant flux incident upon a surface per unit area, E_r is the reflected irradiance, k is a constant specific to the observed shape, α is the bond albedo of the object, and A is the object's cross-section area. Hejduk et al.[4] proposed that by fixing the Sun as the illumination source and utilizing the conversion for Δ_{mag} specified in Eq. 4, the illuminance ratio may be formulated in terms of stellar magnitudes (Eq. 5).

$$\Delta_{mag} = -2.5 \log_{10} \left(\frac{E_r}{E} \right) \quad (4)$$

$$M_v(sat) = -26.74 + \Delta_{mag} = -26.74 - 2.5 \log_{10}(k\alpha Af(\phi)) + 5 \log_{10} R \quad (5)$$

Therefore, the resulting BRDF generated in the OMC is formulated via Eq. 6. The Δ_{mag} of a target is obtained experimentally in the OMC by determining E from a flat-field image taken of a Spectralon panel, while E_r is approximated from an object image taken at the same spatial coordinates and using identical image acquisition parameters as those used with the Spectralon panel (e.g., CCD filter, exposure time, etc.). This measurement is then repeated until a hemisphere about the target is sampled, sufficient to generate an approximation of the BRDF.

$$f_r(\theta_i, \phi_i; \theta_r, \phi_r) = -2.5 \log_{10} \left(\frac{E_r(\theta_i, \phi_i; \theta_r, \phi_r; E_i)}{E(\theta_i, \phi_i)} \right) \quad (6)$$

The BRDF of a target imaged in the OMC may be used to identify an unknown object's material composition by matching an experimentally derived BRDF to its counterpart approximated from telescopic measurements. With the material composition confirmed, the overall geometric albedo, α_g , may be subsequently approximated, and the phase function $f(\phi)$ may also be directly constructed using photometric data collected when sampling the BRDF.

3. DATA / RESULTS

3.1. BRDF Approximation Qualifications

To ascertain the accuracy of acquired spectrometric data and subsequent image analysis processes, a Lambertian sphere was the first target sampled in the OMC. The optical properties of this target are in close parody with a perfectly diffuse surface, and therefore the accompanying approximated BRDF and phase function should exhibit the same predictable characteristics of a diffuse surface.

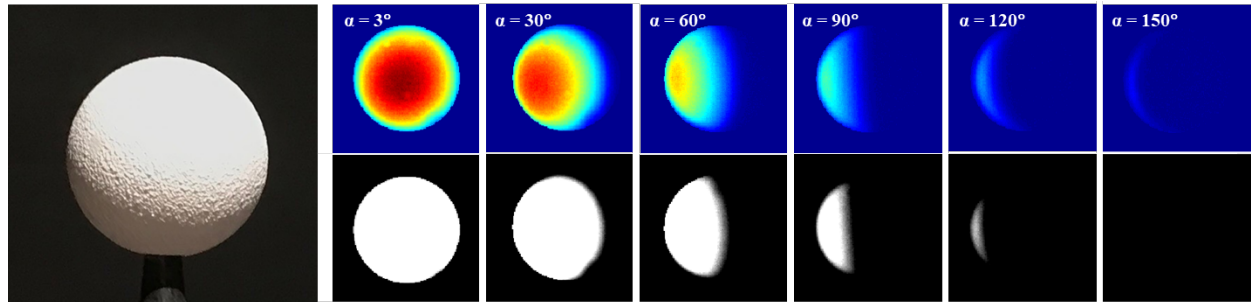


Fig. 3. Lambertian sphere test object (left). Representative binary and color map renderings of captured images of Lambertian sphere across the solar range (right).

The Lambertian sphere, oriented at $\theta=0^\circ$ and $\psi=0^\circ$, was imaged with B, R, and C Johnson/Bessel filters, with a 1-second exposure time for each phase angle (ϕ) in a solar range of 5° to 155° in 5° increments (Fig. 3). The apparent magnitude of each image was then determined using a Spectralon panel as reference, imaged at $\phi = 5^\circ$, $\theta = 0^\circ$, $\psi = 0^\circ$. A phase function of the Lambertian sphere was then generated for each filter and compared with the theoretical phase function for a perfectly diffuse surface (Fig. 4). The Clear intensity and Δ_{mag} curves match closely with the theoretical Lambertian phase function, with only small variances which could be attributed to the physical limitations involved in creating a perfectly-diffuse surface. The R and B filtered functions follow a similar curve, but due to the low exposure time used in the image acquisition, the intensity of these curves is only a fraction of that acquired with C. In the interest of collecting the maximum amount of data in the time allotted, it was decided that all remaining image captures in this study would use a Clear filter with a 1-second exposure time.

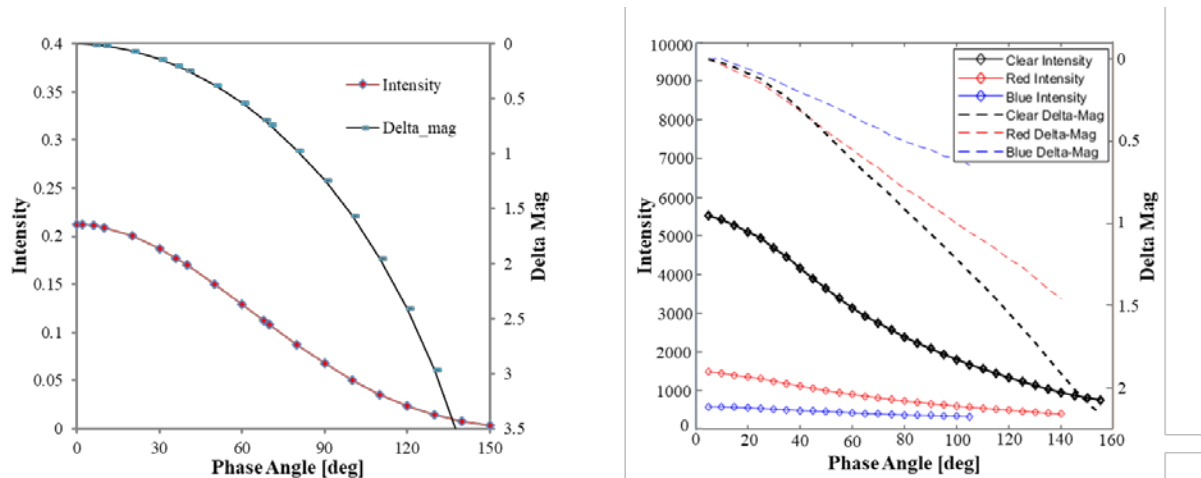


Fig. 4. Theoretical phase function of a perfectly diffuse surface (left). Phase functions generated for Lambertian sphere when imaged through B, R, and C Johnson/Bessel filters (right).

The Lambertian sphere was then imaged in a hemisphere of view orientations comprising 21 combinations of θ and ψ for each phase angle in the same solar range (5° - 155° in 5° increments). The averaged apparent magnitude and corresponding standard deviation of all 21 orientations in the sampled hemisphere is plotted at each phase angle in the solar range in Fig. 5. The averaged apparent magnitude expectedly rises gradually as the phase angle increases, and the corresponding standard deviation in each sampled hemisphere remains low, indicative of a diffuse object. Throughout a majority of the solar range, the Lambertian sphere exhibits a mean standard deviation of 0.0117, constituting an average deviation of the apparent magnitude at each phase angle of 0.15% with a variance of $8.5302e^{-6}$. Unexpectedly however, the standard deviation of the apparent magnitude rises substantially as the phase angle increases beyond 140° . At a phase angle of 155° , the standard deviation grows to a maximum value of 0.12, representing an order of magnitude increase in standard deviation. Despite this dramatic increase, the generated BRDF surface, depicted in Fig. 6, still retains all the attributes of a diffuse surface.

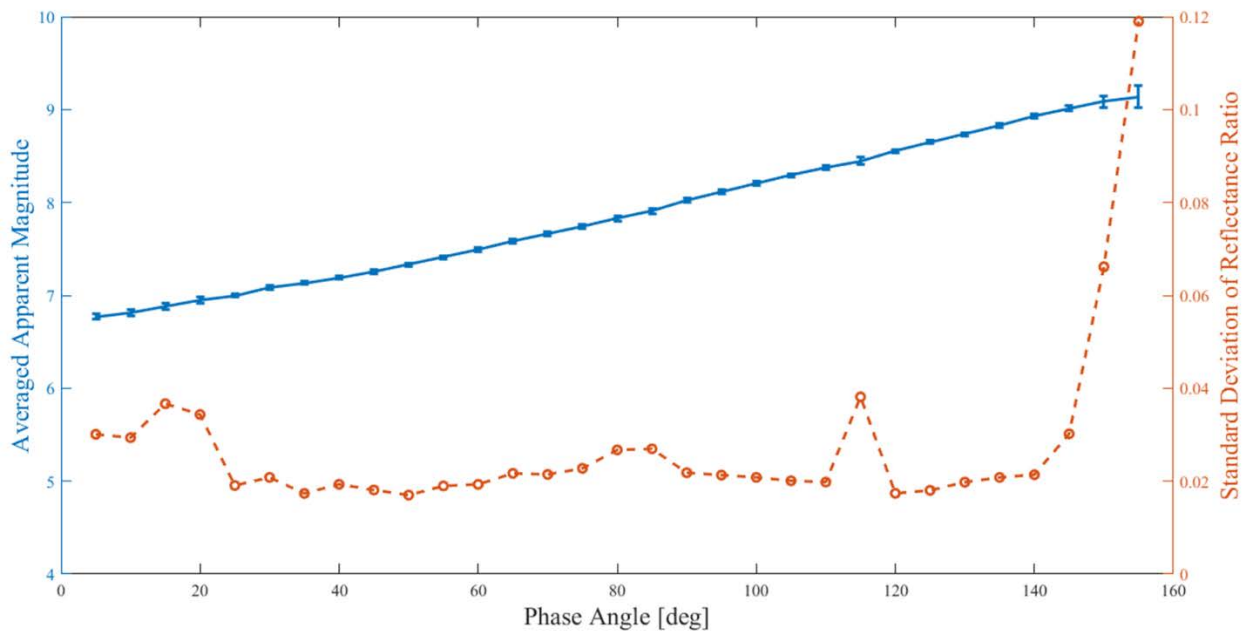


Fig. 5. Averaged apparent magnitude and corresponding standard deviation of Lambertian sphere when imaged through a Clear filter with a 1-second exposure time

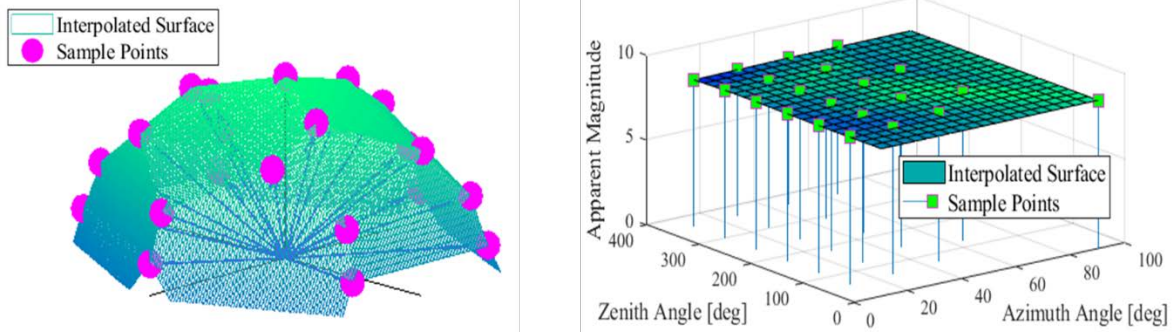


Fig. 6. Approximated BRDF surface fitted to measurements taken from sampled hemisphere of Lambertian sphere at $\phi = 155^\circ$ (left). Corresponding distribution of apparent magnitude measurements (right).

The source of this pronounced increase in standard deviation was investigated; it was initially speculated that at higher phase angles, the decrease in intensity of the target may cause the image processing program to include background objects in the measurement. This notion was quickly dispelled however, as the area measured by the program exhibits the expected exponential decay across the solar range (Fig. 7). Next, it was investigated whether the object was moving in the image frame throughout the duration of image acquisition. The robotic arm used to manipulate the view orientation of the object requires tedious calibration, which if done incorrectly may cause the object's position to vary from one sample orientation to the next. While it was determined that the center of the object did shift by an average of 3.0826 mm across all 21 sampled orientations (Fig. 7), this 'wobble' remained constant throughout the solar range and therefore could not be the source for the pronounced increase in standard deviation. However, it should be noted that this 'wobble' will undoubtedly have an effect on measurements made throughout the solar range, but the impact should be minor. Additionally, given that the robotic arm was calibrated to align with the zenith axis to within 0.1° prior to the acquisition of these images, it seems that the 'wobble' is pervasive.

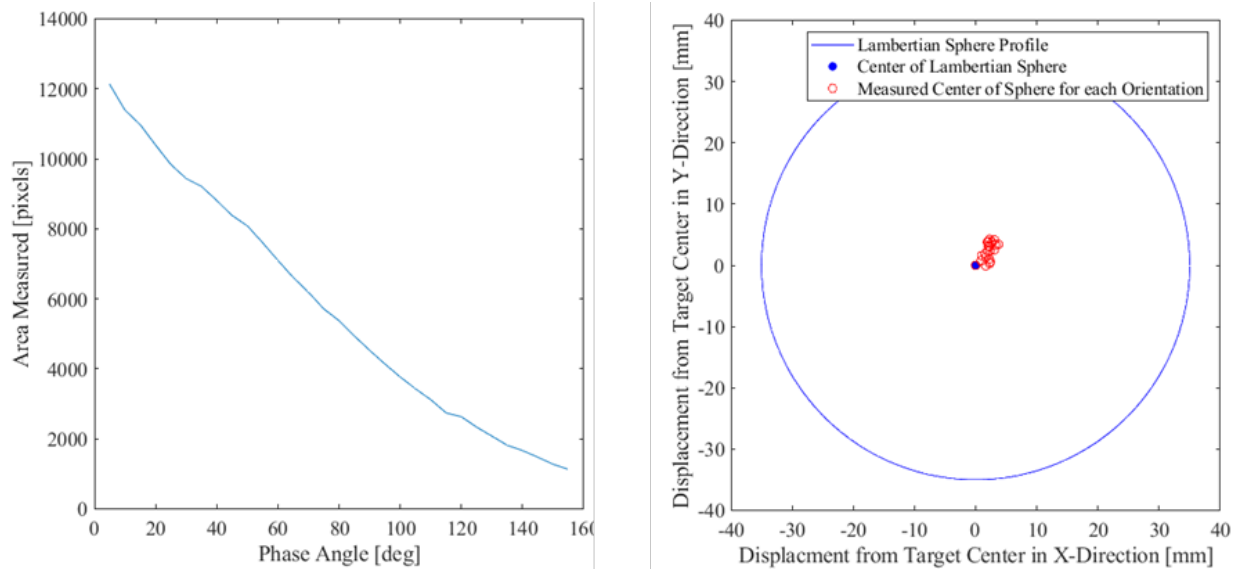


Fig. 7. Area of the image measured for intensity measurements of Lambertian sphere at $\theta=0^\circ$, $\psi=0^\circ$ throughout solar range (left). Locations of perceived center of Lambertian sphere throughout 21 object orientations (right).

Finally, the source of the anomalous increase in standard deviation was identified to be the Lambertian target itself. As shown in Fig. 8, there are two pockmarks on the surface of the sphere. While the site labeled 'A' in Fig. 8 created small intensity fluctuations, the location of site 'B' was such that the profile of the pockmark was exposed on the edge of the sphere when the target was oriented at $\psi = 60^\circ$ at θ angles greater than 60° . While the phase angle was $\leq 140^\circ$, the angle of the incident light was such that the profile of these pockmarks was largely obscured, save for the local peaks in standard deviation at phase angles of 5° , -20° , and 115° , where the pockmarks were revealed as shallow

craters. However, as the phase angle increased beyond 140° , a sliver of the backlit hemisphere was visible through the profile of site 'B', creating a spike in the intensity measurement and resulting in the subsequent increase in standard deviation.

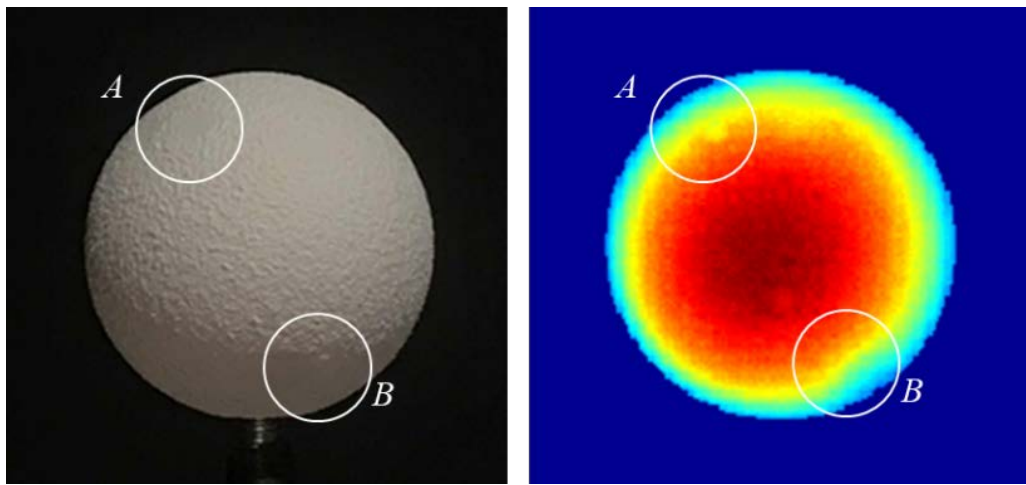


Fig. 8. Lambertian target with pockmark sites 'A' and 'B' (left) and corresponding intensity distribution generated from image (right). Target orientation: $\phi = 5^\circ$, $\theta = 0^\circ$, $\psi = 0^\circ$

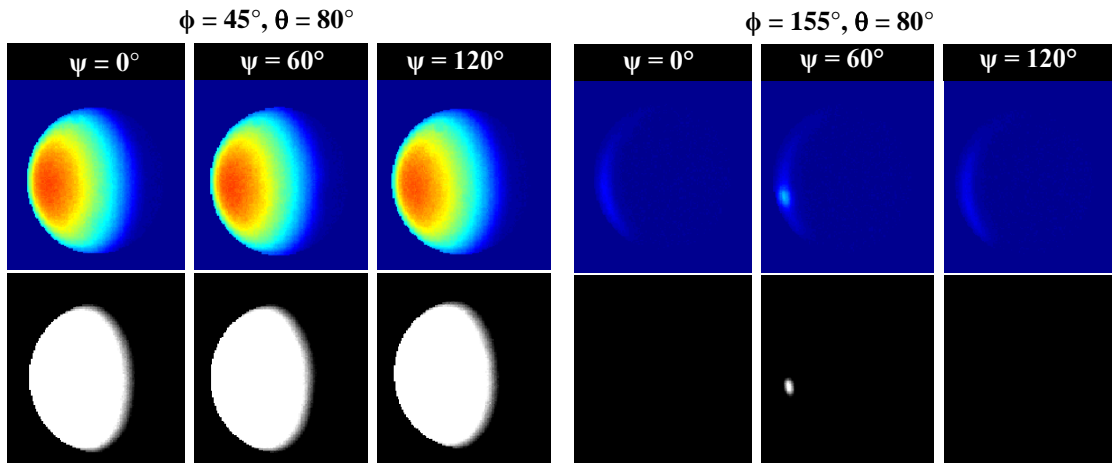


Fig. 9. Lambertian sphere imaged at $\alpha = 45^\circ$ with no intensity abnormalities (left). Lambertian target imaged at $\alpha = 155^\circ$ with intensity spike visible at $\phi = 60^\circ$ due to pockmark site 'B' (right).

3.2. Phase Functions

Having confirmed the validity of generated BRDF and phase function approximations, several spherical targets were then imaged to investigate whether the optical properties of a target can be discerned using the phase function. Therefore, a matte aluminum sphere, a felt pool ball, a polished aluminum sphere, and a disco ball were imaged at $\theta=0^\circ$, $\psi=0^\circ$ for $\phi=5^\circ$ - 155° in 5° increments using a clear filter and 1-second exposure time (Figs. 10-13).

Despite all four targets sharing the same shape factor, k , distance to observer, R , and the matte and polished aluminum spheres sharing the same cross-sectional area, A , the phase functions generated for all four targets were found to be both unique and repeatable. Additionally, the characteristics of each target's phase function were found to contain indicators as to the specular and/or diffuse behavior of each target's surface. A diffuse target's phase function was found to have a very smooth intensity curve, generally with an exponentially decreasing intensity as the phase angle approached 90° . The corresponding diffuse Δ_{mag} curve decreases logarithmically throughout the entire solar range. In comparison, a specular phase function is much more discontinuous, with local jagged peaks present whenever the ray

geometry is such that light from the target is reflected into the CCD; the Δ_{mag} curve was found to match the intensity curve's shape almost exactly.

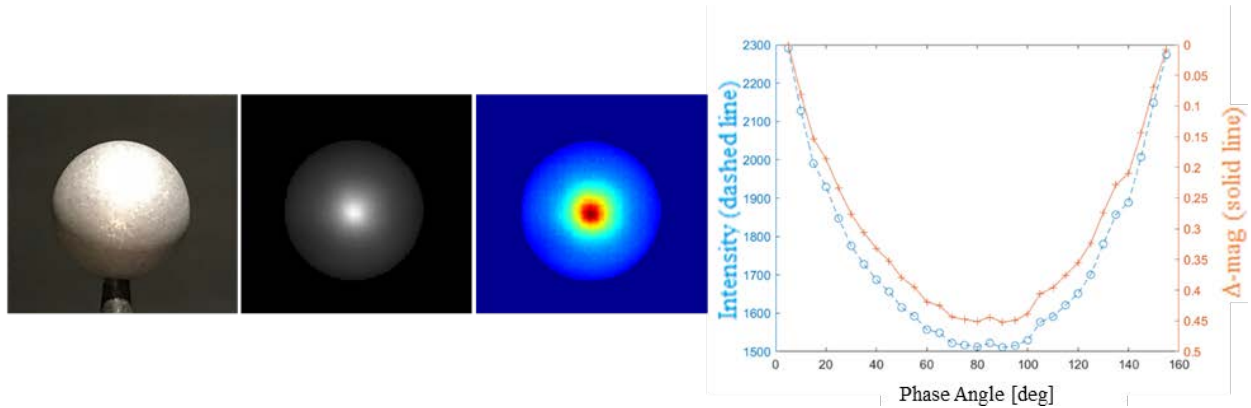


Fig. 10. Matte aluminum sphere with varying optical surface properties and corresponding phase function

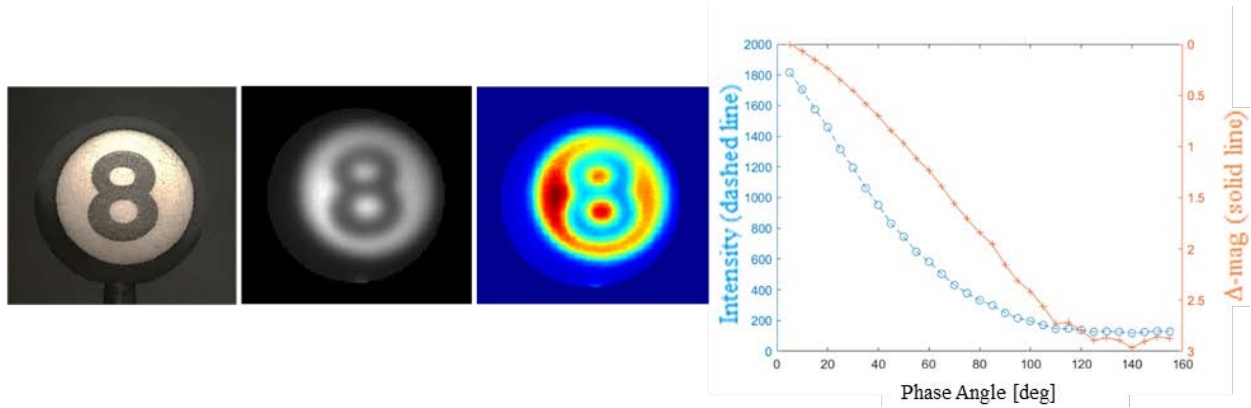


Fig. 11. Felt pool ball with diffuse surface properties and corresponding phase function

The matte aluminum sphere (Fig.10) exhibits a quadratic phase function, decreasing quadratically until an inflection point is reached at a phase angle of $\sim 85^\circ$. While both the intensity and Δ_{mag} curves are continuous, the close adherence of the Δ_{mag} curve to intensity, coupled with the exponential increase of intensity in the second half of the solar range, suggests that this target has a surface with both specular and diffuse characteristics. The felt pool ball exhibits a strongly diffuse phase function as expected, made evident in the characteristic shape of the intensity curve (Fig.11). The Δ_{mag} is initially very smooth but begins to fluctuate as the phase angle increases beyond 85° . This is believed to be due to the various states of illumination of the white and black coloring around the number on the face of the pool ball.

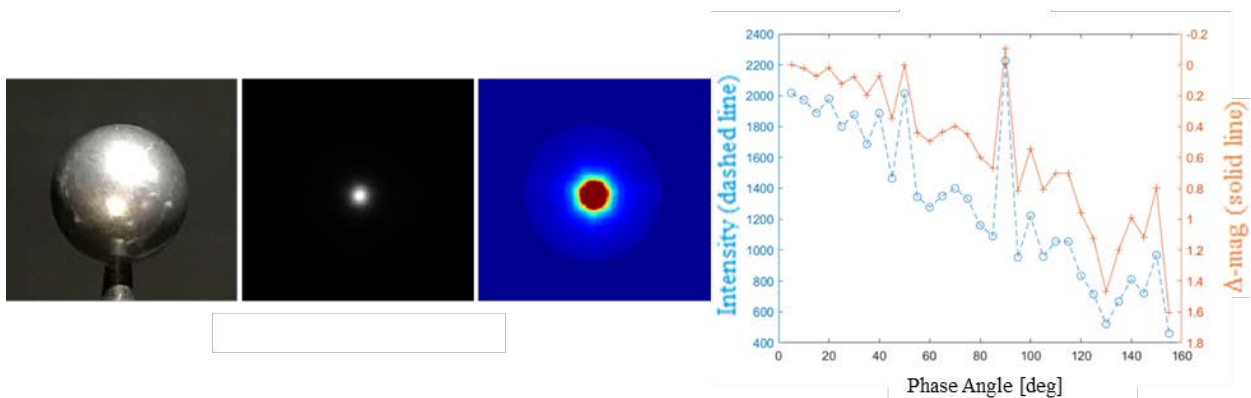


Fig. 12. Polished aluminum sphere with specular surface properties and corresponding phase function

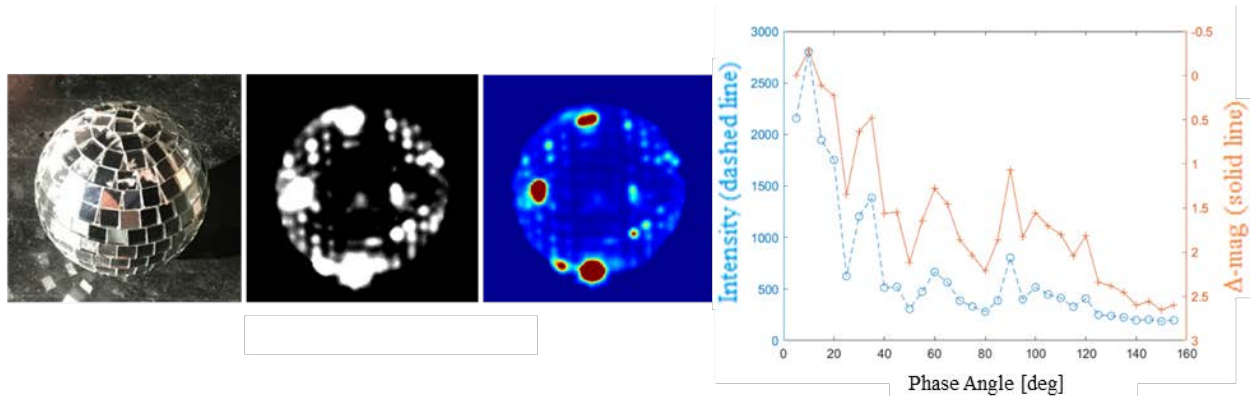


Fig. 13. Disco ball with specular surface properties and corresponding phase function

Unsurprisingly, the polished aluminum ball's phase function is very specular (Fig.12). The erratic phase function has matching jagged peaks in the intensity and Δ_{mag} curves that decrease slightly over the span of the solar range. The disco ball is also strongly specular with a similar characteristically jagged phase function (Fig.13). However, the local peaks in intensity and Δ_{mag} decay in magnitude as the phase angle increases happen much more quickly than with the polished aluminum ball. This is likely due to the faceted geometry of the object's surface; as the phase angle increases beyond $\sim 35^\circ$, the ray geometry is such that there are fewer facets oriented so as to reflect light into the CCD.

The ability to discern the optical behavior of a target from its phase function via easily identifiable characteristics in the intensity and Δ_{mag} curves is a very promising finding, suggesting that the material of a tracked object may be made more readily identifiable by its spectral and/or diffuse behaviors. In some cases, such as with the felt pool ball, the phase function potentially may even be used to verify the presence of colored patterns or markings on the body's surface. While much more investigation into the effects of varying a target's optical and geometrical properties on the behavior of the phase function is required, these preliminary findings suggest that such work would certainly be a worthwhile endeavor.

4. SUMMARY

The BRDF and phase function approximations generated in the OMC have been validated using a Lambertian sphere as a test object, with any deviations in the approximated functions from the perfectly diffuse test-case having been found attributable to features on the surface of the test object itself. After the process was validated, several spheres with various surface optical properties but identical shape factors, k , distance to observer, R , and in two cases identical cross-sectional areas, A , were imaged and the corresponding phase functions were found to be unique and repeatable. Additionally, it was found that the optical properties of each target's surface are easily discernable in its phase function due to identifiable specular and diffuse behaviors manifested in the intensity and Δ_{mag} curves (i.e., continuity of intensity curve and degree of symmetry between intensity and Δ_{mag} curves).

Further work is planned to investigate how varying a target's shape affects the approximated BRDF and phase function, specifically in conjunction with changes in the target's material. Representative samples of orbital debris are intended to be imaged, including samples of carbon/glass fiber-reinforced polymers, multi-layered insulation, solar cells, and fragments resulting from hypervelocity impact experiments. Characteristics in the subsequent phase function approximations will be sought in the hopes that there are similarly discernable traits in the intensity and Δ_{mag} curves, which may identify an object's shape and material composition. Also, plans are to attempt to fit existing BRDF models to data collected in the OMC to investigate whether the coefficients obtained in the fit are unique and repeatable; if so, this may be an invaluable tool for on-going characterization of the orbital debris environment. Further work intends to explore the incorporation of ray-tracing software to analyze combinations of photometric variables, narrowed down from an initial screening of the phase function and BRDF, until a solution of material composition, size, distance, etc., is obtained which closely fits the empirical photometric data. While this paper constitutes only an initial foray into the classification of orbital debris via BRDF and phase function analysis, it seems that the prospect of developing a suite of tools in the OMC capable of identifying and cataloging previously unidentifiable orbital debris is tantalizingly promising.

5. REFERENCES

- [1] H. Cowardin, M. Mulrooney, S. Lederer, J.-C. Liou. “Optical signature analysis of tumbling rocket bodies via laboratory measurements,” AMOS, 11-14 Sept 2012.
- [2] E. Barker, et al., “Analysis of Working Assumptions in the Determination of Populations and Size Distributions of Orbital Debris from Optical Measurements,” Proceedings of the 2004 AMOS Technical Conference, Wailea, Maui, HI, pp. 225-235, 2004.
- [3] F.E. Nicodemus, et al., *Geometrical Considerations and Nomenclature for Reflectance*, Washington National Bureau of Standards, US Department of Commerce, 1977.
- [4] M.D. Hejduk, H.M. Cowardin, and E.G. Stansbery, “Satellite Material Type and Phase Function Determination in Support of Orbital Debris Size Estimation,” 2012 AMOS Technical Conference, Maui, Hawaii, 11-14 Sept 2012.